DOI: 10.1021/ma100601x

Macromolecules
ARTICLE

Effects of Film Instability on Roughness Correlation and Nanodomain Ordering in Ultrathin Films of Asymmetric Block Copolymers

Ya-Sen Sun,*,† Shih-Wei Chien,† and Pin-Jiun Wu‡

†*Department of Chemical and Materials Engineering, National Central University, Taoyuan 32001, Taiwan, and* ‡*National Synchrotron Radiation Research Center, Hsinchu 30077, Taiwan*

Received December 11, 2009; Revised Manuscript Received April 29, 2010

ABSTRACT: We investigated the dewetting, surface roughness, and ordering of cylindrical nanodomains in polystyrene-*block*-poly(methyl methacrylate), P(S-*b*-MMA), ultrathin films of approximately monolayer thickness on bare silicon substrates (SiO_x/Si) and substrates coated with end-grafting PMMA (PMMA-SiO_x/Si) and PS (PS-SiO_x/Si) homopolymers. For films with asymmetric wetting boundaries on SiO_x/Si and PMMA-SiO_x/Si, annealing caused relief structures (holes and islands) locating on top of an underlying P(S-*b*-MMA) wetting monolayer. The interfaces of the destabilized thin films on polar substrates have a smooth free surface. In addition, a surface undulation in film thickness to achieve the commensurability of film thickness with the nanodomain spacing facilitates the ordering of internal nanostructures. In contrast, for symmetric wetting boundaries on PS-SiO_x/Si, thin films that resisted dewetting on a PS brush have a rough free surface. In the absence of undulations in thickness, a perturbation, as result of chain stretching, in the interdomain spacing yielded small in-plane randomly oriented monograins on PS-SiO_x/Si. Consequently, the free surface roughening was allowable to occur due to preferential segregation of excluded polymer chains from monograin boundaries onto the free surface. Finally, we demonstrate that the roughnesses between the interfaces of the wetting monolayer are correlated.

Introduction

Because their various complicated morphologies order on a nanometer scale, block copolymers (BCP) offer diverse and versatile benefits as potential nanotechnological applications, such as masks for lithography and templates for the fabrication of metallized nanowire/nanodots.[1−8] Those nanotechnological applications generally depend on thin films being used as the nanostructured materials. To implement these applications, a precise control over nanostructure, orientation, and order in thin films is important, which requires the use of external fields, such as electric fields,[6] graphoepitaxy,[9,10] crystallization,[11−14] controlled interfacial interactions,[15,16] chemically patterned substrates,[5,17,18] solvent evaporation, and annealing.[19−21] Modifying a substrate with chemical or topographic patterns is widely used to tailor over the nanodomains and their spatial and orientational order in thin films.[5,9,10,17,18]

In addition, BCP thin films have more diverse morphologies than bulk samples because of interfacial interactions (at BCP/air and BCP/substrate interfaces) and thickness commensurability.[22−29] Thin films of symmetric copolymers have been intensively studied.[24−29] In most cases of symmetric thin BCP films on preferential surfaces having strong interactions with either block, the lamellae preferentially align parallel to the substrate surface with symmetric and asymmetric wetting. Asymmetric versus symmetric wetting is controlled by favorable interactions with both interfaces by each block, in which the block with the smaller surface energy resides typically at the free surface. If the initial thickness (h) of a thin film is incommensurate with the natural length scale (L) of microphase-separated nanodomains, the thin films are metastable. Upon annealing at high temperatures or exposing with solvent vapors, the surface undulation in a thin film produces islands or holes with their heights quantized as either $(n + {}^1/_2)L$ for asymmetric wetting or as nL for symmetric wetting, in which n is an integer.[24−26] In contrast, BCP thin films on neutral surfaces have nanodomains that orient normal to the substrate interface because of a lack of preferential interactions with substrates by either block.[16,29−31]

Spin-coating is widely used to prepare thin polymer films on solid substrates. The rapid evaporation of a solvent during spin-coating inevitably produces frozen-in nonequilibrated morphologies of polymers.[32] To promote an equilibrium morphology, thin films are commonly subjected to annealing. External disturbances from thermally excited capillary waves inevitably lead, however, to surface undulation in the thin films (i.e., rupture and subsequent dewetting of thin films) as long-range intermolecular forces become dominant when the thin films have a thickness of order 10^{-7} m .[33,34] As a result, various morphologies resulting from dewetting—discrete cylinder holes, droplets, and interconnected patterns—are typically observed in the destabilized films.[34−38] Such morphologies depend on the nature of long-range van der Waals forces and short-range polar intermolecular interactions between a polymer and a substrate.[37,38] Much is known about the dewetting behavior of homopolymers on solid or liquid nonwetting substrates, as summarized in recent review articles.[39,40] In addition to a large-scale surface undulation of film thickness (i.e., dewetting) upon heating, the roughness at both interfaces of a thin film reveals variations on a short-scale order with duration and temperature of annealing. Characterizing with X-ray reflectivity and diffuse X-ray scattering, Müller-Buschbaum et al. found that the roughness at both interfaces of a spin-coated film, of thickness of order a few nanometers, replicated the substrate roughness, but heating caused a decay of the roughness replication.[41,42]

Experiments have focused mainly on the dewetting of simple polymeric liquid films[34−40] or dewetting of symmetric BCP

*To whom correspondence should be addressed. E-mail: yssun@cc.ncu.edu.tw.

 Published on Web 05/12/2010

thin films.[43−47] Little is understood about dewetting and the interfacial roughness of asymmetric BCP thin films. Furthermore, in most investigations of the surface topographies of thin polymeric films on a substrate, only measurements by atomic force microscopy (AFM) or optical microscopy (OM) were performed; the structural study was thus limited to the polymer−air interface.[43−48] Because polystyrene-*block*-poly(methyl methacrylate) (P(S-*b*-MMA)) BCP are prospective materials for nanolithography, much effort is devoted to control the domain orientation in P(S-*b*-MMA) thin films with surface fields,[4−21,49−51] but little attention is paid to the influence of film instability on nanostructures at interfaces and buried structures within the thin films that dewet substrates.[49,50] In this work, we investigated thin destabilized films of asymmetric (P(S-*b*-MMA)) as a model to understand both the surface roughness at interfaces and the buried internal nanostructures and nanodomain ordering in P(S-*b*-MMA) ultrathin films. To induce the dewetting, nonisothermal annealing at a heating rate 1 °C/min from 30 to 245 °C was imposed on the thin films. In the following report, we first show the surface topographies of P(S-*b*-MMA) films of varied thickness after nonisothermal annealing was imposed on films spread on substrates of three kinds: a bare Si substrate and a modified Si substrate by end-grafting PMMA and PS brushes, respectively, denoted SiO_x/Si, PMMA-SiO_x/Si, and PS-SiO_x/Si for brevity. Next, we demonstrate the interfacial roughness, nanodomain spacing, and ordering in the destabilized thin films by means of X-ray reflectivity and diffuse scattering. Finally, we discuss in detail the influence of film instability on the cylindrical nanodomain spacing, the ordering, and the roughness correlation at interfaces.

Experiments

Materials. Hydroxyl-terminated polystyrene (PS-OH, M_n = 6 kg/mol, index of polydispersity I_p = 1.07), hydroxyl-terminated poly(methyl methacrylate) (PMMA-OH), M_n = 6 kg/mol, I_p = 1.06), and polystyrene-*block*-poly(methyl methacrylate) (P(S-*b*-MMA), M_n = 82 kg/mol, f_{ps} = 72% and f_{PMMA} = 28%, I_p = 1.07) were purchased (Polymer Source, Inc.) and used as received.

Surface Modification of Substrate, Film Preparation, and Annealing. Bare silicon wafers were cleaned in a piranha solution (3:7 v/v 30% H_2O_2:H_2SO_4) at ambient temperature for 40 min, rinsed with deionized water, and dried under flowing N_2. PS-OH and PMMA-OH solutions (1 mass % in toluene) were spin-coated (4000 rpm, 1 min) on silicon wafers. The irreversibly grafted layers resulted from annealing (160 °C for 2 days) spin-coated films on hydroxylated silicon wafers under vacuum. Nongrafted materials were removed by sonication in toluene, followed by drying the substrates under flowing N_2. The PS and PMMA layers grafted onto SiO_x/Si possess high thermal stability even after the process of nonisothermal annealing. (see Figure S1 of the Supporting Information). P(S-*b*-MMA) thin films of varied thickness (h), 32.1, 36.4, and 38.3 nm, were prepared via spin-coating (5000 rpm, 30 s) from toluene solutions of varied concentrations (1.4, 1.5, and 1.6 mass % in toluene). The P(S-*b*-MMA) films on SiO_x/Si, PS-SiO_x/Si, and PMMA-SiO_x/Si substrates were dewetted with post-slow heating (1 °C/min) the samples from 30 to 245 °C in a closed hot stage (HCS402 Instec) purged with N_2. When the temperature reached the target, 245 °C, the thin films in their thermally induced morphologies were frozen on quenching into liquid N_2. As the temperature at which the samples were stored is much less than the glass transition temperatures of the PS and PMMA blocks, the morphologies resulting from dewetting showed no change during protracted periods of sample storage.

Topographies of Thin Films by Optical Microscopy (OM) and Atomic Force Microscopy (AFM). To determine the nanodomains, surface roughness, and dewetting morphologies, we investigated the surface of the thin films by AFM (SPA400 Seiko) in the tapping mode. AFM images with scan ranges between 2 μm × 2 μm and 5 μm × 5 μm were recorded. We used aluminum-coated silicon cantilevers of length 125 μm, width 30 μm, and thickness 4 μm. The force coefficient is ∼42 N/m, and the resonant frequency is 330 kHz. Measurements by OM (Olympus BX-BLA2) were performed in the reflection mode.

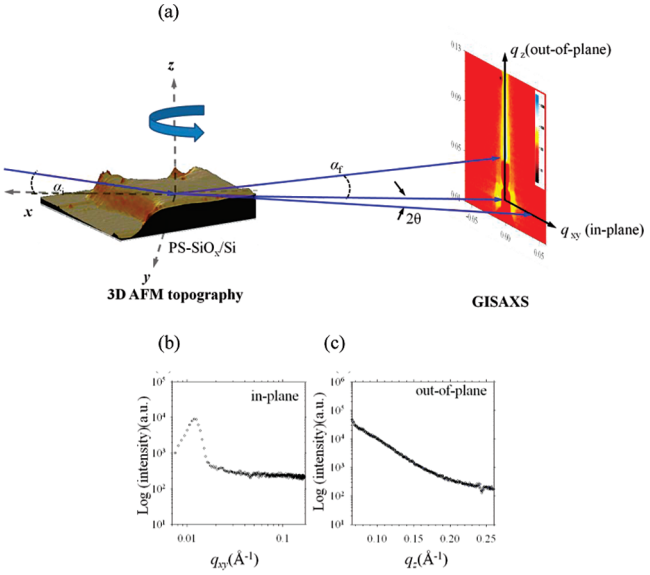

Figure 1. (a) Schematic drawing of the experimental GISAXS setup used at beamline BL23A. The sample is placed horizontally. Shown is a 3D AFM topographic image revealing a dewetting hole in the P(S-*b*-MMA) film of thickness 34.3 nm. The angle of incidence is α_i, and the exit angle is α_f. Intensity dependence as a function of q_{xy} along one horizontal line representing an in-plane scan cut (b). The vertical slice represents an out-of-plane scan cut (c), showing a plot of the dependence of intensity on q_z.

X-ray Reflectivity (XR) and Grazing-Incidence Small-Angle X-ray Scattering (GISAXS). Before XR and GISAXS characterizations, we subjected all thin films to annealing as described above. The reflectivity measurements were performed with a X-ray source (λ = 1.54 Å), with samples placed horizontally. The GISAXS experiments were performed at beamline BL23A of the National Synchrotron Radiation Research Center (NSRRC), Hsinchu. The configuration of the GISAXS at BL23A was detailed elsewhere.[52] A monochromatized X-ray radiation source of energy 10 keV (wavelength, λ = 1.24 nm) and a two-dimensional gas detector with a pixel array 512 × 512 were used to collect 2D GISAXS patterns. The distance from the sample to the detector was 2447.54 mm. The scattering vector, q ($q = 4\pi/\lambda \sin\theta$), with scattering angle θ, in these patterns was calibrated with silver behenate. The films were mounted on a z-axis goniometer. The angle of incidence of each X-ray beam was α_i = 0.17°, which is between the critical angles of the P(S-*b*-MMA) films and the silicon substrates ($\alpha_{c,f}$ and $\alpha_{c,s}$). Scattering angles were corrected for the positions of X-ray beams reflected from the silicon substrate interface with varied incidence angle α_i. 2D GISAXS patterns were typically collected for 180−300 s. The experimental GISAXS geometry is depicted schematically in Figure 1. We performed GISAXS measurements at an angle of incidence greater than the critical angle of total reflection of the P(S-*b*-MMA) films. As an example, Figure 1a shows the anisotropy of the observed scattering pattern of a P(S-*b*-MMA) film of initial thickness 34.3 nm on a PS-SiO_x/Si substrate. The pattern reveals rodlike scattering typical of strongly textured fiber films with cylindrical symmetry, indicating that the cylindrical PMMA nanodomains aligned with a single orientation on top of PS-SiO_x/Si.[53]

Typical characteristics (Bragg rods/spots and Kiessig fringes) of one-dimensional (1D) scattering intensity are clearly

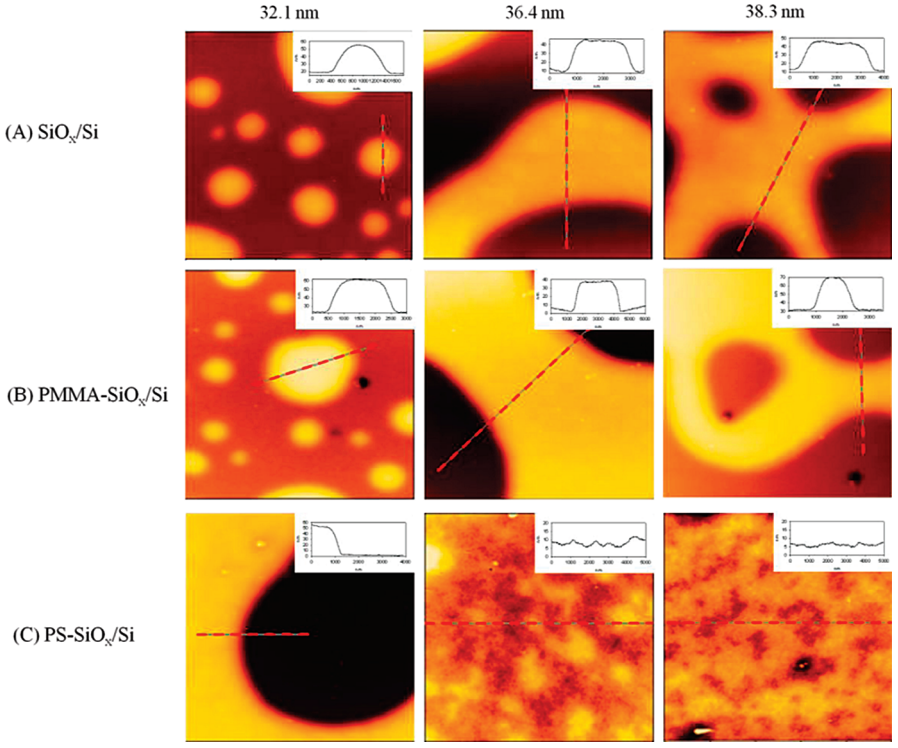

Figure 2. $5 \times 5\ \mu m^2$ AFM height images for P(S-*b*-MMA) films of initial thickness 32.1, 36.4, and 38.3 nm spread on substrates of three kinds: (A) SiO_x/Si, (B) PMMA-SiO_x/Si, and (C) PS-SiO_x/Si, after annealing. Insets show cross sections of the 2D images. The line scans were generated by choosing a random scan line. Dotted lines were plotted for guiding eyes.

observed when the in-plane and out-of-plane scan cuts were imposed on the 2D GISAXS pattern to show the 1D profiles.[54] An in-plane profile was obtained with intensity scanning on varying q_{xy} at a given q_z whereas an out-of-plane profile at $q_{xy} = 0$ was obtained with a vertical slice of intensity as a function of q_z. Typical slices are indicated in Figure 1a with a horizontal line and vertical one. The corresponding in-plane 1D GISAXS profile shown in Figure 1b reveals a Bragg peak, of which the diffraction position is associated with a periodic spacing of nanodomains. Figure 1c shows the out-of-plane GISAXS profile with intensity dependence along the line at $q_{xy} = 0\ Å^{-1}$. The Yoneda and reflection peaks along the thickness direction at $q_{xy} = 0\ Å^{-1}$ were shielded with a beam stopper to prevent the detector from radiation damage due to an intense reflection beam; both Yoneda and reflection peaks are consequently absent from the 1D out-of-plane profile of GISAXS. The only scattering feature shows modulations of which the period relates to the thickness of the P(S-*b*-MMA) film (or the underlying PS-OH brush).

Results and Discussion

Topographical Features and Dewetting Mechanisms: Islands and Holes. Depending on the initial thickness of the film, distinct dewetting morphologies were observed after thin films on SiO_x/Si, PMMA-SiO_x/Si, and PS-SiO_x/Si substrates were subjected to annealing, as shown in Figure 2A−C (cf. the OM images in Figure S2 for large-scale morphological observations). Upon dewetting with annealing, on the SiO_x/Si and PMMA/SiO_x/Si substrates the P(S-*b*-MMA) films exhibited varied topographic microstructures ranging from islands to holes. For the initially thinnest film 32.1 nm, a polydispersive population of islands (drops) is present on the SiO_x/Si and PMMA-SiO_x/Si substrates (Figure 2A,B). In addition to the larger drops, the surface of the initially thinnest film was covered also with a high density of small droplets, of which the dimensions were in the range of tens of nanometers. This observation indicates that dewetting nucleates via formation of a random distribution of droplets rather than via formation of holes. For the films of initial thickness 36.4 and 38.3 nm, holes were typically formed on SiO_x/Si on dewetting via a nucleation and growth mechanism. The cross sections of the AFM topographies demonstrate that the height of relief structures (drops and flatten areas between holes) is approximately 38−40 nm, which length is very comparable to the intercylinder distance (D) of a P(S-*b*-MMA) bulk sample.[55] Furthermore, the P(S-*b*-MMA) films dewetted more quickly on PMMA-SiO_x/Si than on SiO_x/Si. The P(S-*b*-MMA) films that dewetted on SiO_x/Si had holes. For comparison, the films with initially similar thickness (36.4 and 38.3 nm) spread on top of PMMA-SiO_x/Si reveal that holes grew with time to form a network, and eventually a part of the network broke into droplets. In contrast to those films on SiO_x/Si and PMMA-SiO_x/Si substrates, the P(S-*b*-MMA) films on a dense PS brush showed mild dewetting, as shown in Figure 2C.

Film Thickness and Roughness. Prior to annealing, the P(S-*b*-MMA) films show pronounced fringes with only one period of oscillation, $\Delta Q_z = 2\pi/h$; h denotes the thickness of a film (cf. Figure S3). Upon heating, the period of oscillation alters. Figure 3 shows data for the X-ray reflectivity of P(S-*b*-MMA) films of three initial thicknesses on SiO_x/Si (A), PMMA-SiO_x/Si (B), and PS-SiO_x/Si (C) substrates after those films were subjected to annealing. A decrease in the frequency of oscillation is observable for the film that dewetted to form droplets. This decreasing frequency implies that the film became "thinner" (ca. 21 nm) than its initially as-spun thickness (32.1 nm). The reason is that X-rays are "blind" to the thickness of the droplets because the droplets that are in contact with the surrounding air show no density contrast from air; however, X-rays can detect the thickness of the P(S-*b*-MMA) monolayer that is anchored on a solid surface with PMMA blocks at the solid-monolayer surface and with PS blocks facing outward.[44]

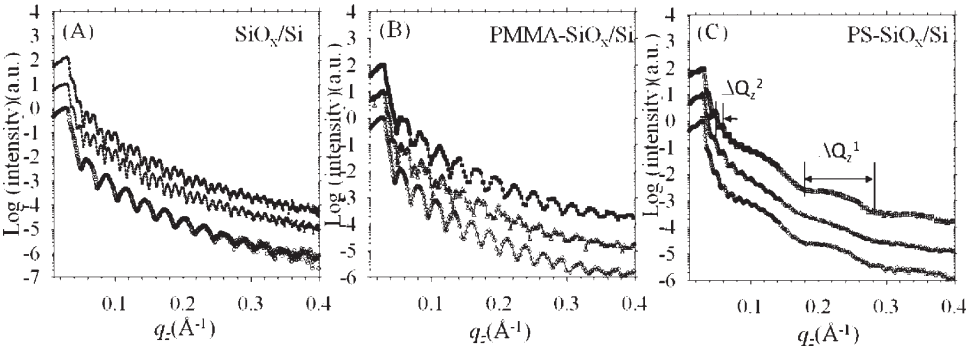

Figure 3. X-ray reflectivity data vs q_z for P(S-*b*-MMA) films of initial thickness 32.1 nm (bottom curves), 36.4 nm (middle curves), and 38.3 nm (top curves), spread on substrates of three kinds: (A) SiO_x/Si, (B) PMMA-SiO_x/Si, and (C) PS-SiO_x/Si, after annealing. For clarity, the curves are shifted relative to each other by 1 decade.

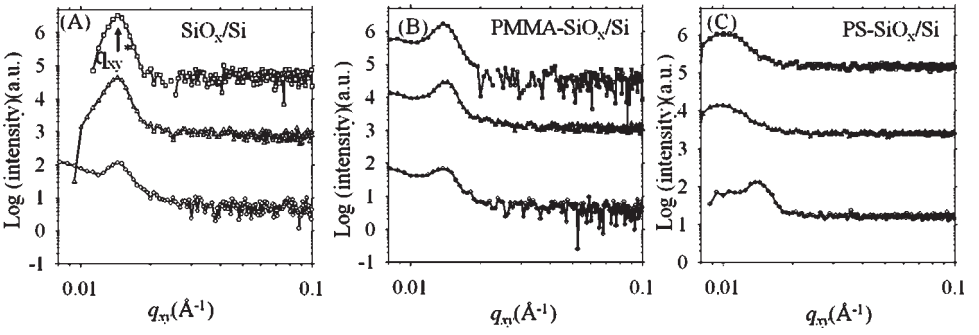

Figure 4. 1D in-plane profiles of GISAXS for P(S-*b*-MMA) films of initial thickness 32.1 nm (bottom curves), 36.4 nm (middle curves), and 38.3 nm (top curves), spread on substrates of three kinds: (A) SiO_x/Si, (B) PMMA-SiO_x/Si, and (C) PS-SiO_x/Si, after annealing. For clarity, the curves are shifted relative to each other by 1 decade.

This result indicates that the droplets appear dispersed on a sea of surface-induced ordered P(S-*b*-MMA) monolayer after the temperature was raised to 245 °C. A qualitatively different trend, showing an increase in the frequency of oscillation with thermal annealing, emerged from the films in which nucleation and growth of holes occurred within the layer matrix. We attribute the increasing frequency to indicate an increased overall thickness of the films. The reason is explained as follows: as the films dewetted to form holes, on a basis of conservation of mass the film thickness between the holes increased.[35] In contrast, as spun on top of PS-SiO_x/Si, the annealed films reveal fringes in a series with two periods of oscillation (Figure 3C). The low-frequency fringes (ΔQ_z^1) attributed to the thickness of a dense PS brush are clearly observable, whereas the high-frequency fringes (ΔQ_z^2) corresponding to the thickness of P(S-*b*-MMA) are rapidly damped. Since the X-ray reflectivity detects the layer thickness, the density contrast, and the interfacial roughness thickness,[56] the damping of fringes is mainly attributed to different roughness thicknesses at the film−air and film−substrate interfaces. Thus, the rapid damping of the high-frequency fringes indicates that the interfaces of the P(S-*b*-MMA) films on top of PS-SiO_x/Si have different surface roughness thicknesses. By contrast, the underlying layer of PS brush has identical interfacial roughnesses. Similarly, identical interfacial roughnesses were also observed for the destabilized P(S-*b*-MMA) films on SiO_x/Si and PMMA-SiO_x/Si.

It should be noted that none of the oscillations, as shown in Figure 3B, are due to the PMMA layer used for surface modification. A strong affinity between the polar carboxyl groups of PMMA chains and the hydroxyl surface of the silicon wafer hindered the hydroxyl-terminated ends of PMMA from completely grafting to the underlying substrates; homogeneous grafting of PMMA-OH is hence not readily achieved upon annealing at 160 °C in vacuum for 2 days. After unbound PMMA-OH was removed by sonication in toluene, a few hydroxyl sites (unbound by PMMA) remained exposed on the surface of the SiO_x/Si substrates. As a result, the presence of the hydroxyl sites enabled a further polar−polar interaction with the carboxyl groups of PMMA, which is unfavorable for the formation of a brush conformation of PMMA chains because of a low grafting density. Therefore, the grafted PMMA layer is unstable against penetration of the PMMA block of P(S-*b*-MMA) so that a P(S-*b*-MMA) monolayer of ca. 22 nm is allowable to contact and to anchor the substrate through the grafted PMMA layer. As a result, the layer of grafted PMMA homopolymer chains is nonuniform in thickness. This is explained why fringes corresponding to the PMMA layer are not discernible.

Ordering of Cylindrical Nanodomains. To detect the formation of nanodomains, we implemented the in-plane scan cuts on the 2D GISAXS patterns (cf. Figure S4) to show the 1D scattering profiles. Figure 4 reveals the 1D in-plane GISAXS profiles for the same P(S-*b*-MMA) films of varied thickness on SiO_x/Si, PMMA-SiO_x/Si, and PS-SiO_x/Si after annealing. As can be seen in Figure 4, the P(S-*b*-MMA) thin films on SiO_x/Si and PMMA-SiO_x/Si reveal a Bragg peak. Since only a monolayer thickness of P(S-*b*-MMA) was spin-coated on substrates, the absence of high-order Bragg peaks implies that the formation of perpendicular-oriented PMMA cylinders with a hexagonal packing on the substrates is excluded. Only one layer of the parallel-oriented PMMA nanocylinders formed within the P(S-*b*-MMA) films contributes to the principal Bragg peak. Therefore, the diffraction position is associated with an intercylinder spacing.

As shown in Figure 4A,B, such a Bragg peak for the P(S-*b*-MMA) films on SiO_x/Si and PMMA-SiO_x/Si presents an invariant in the q_{xy} position ($q_{xy}^* = 0.0142$ Å^{-1}) irrespective of the initial thickness. In contrast, the P(S-*b*-MMA) thin films on top of PS brush reveal the in-plane diffraction peak with small intensity and broadening, indicative of a poor ordering of nanodomains within the P(S-*b*-MMA) films (Figure 4C). The poor ordering results from increased stretching of the polymer chains made evident by a shift in the diffraction position to smaller q_{xy}.

In thin films of block copolymers, of which the initial thickness is incommensurate with the long periods of nanodomains, dewetting creates holes and islands that reflect variations in the film thickness. Once the holes and islands develop from the surface undulations, the films split into two regions, with each being commensurate with the long periods of the nanodomains.[57] As a result, the ordering of nanodomains within the film became improved. If barriers to form islands and holes are so great that the film rupture is less likely, it is more favorable to perturb the nanodomain periodicity so as to form in-plane randomly oriented monograins with a short average domain length than to form islands or holes.[27−29,58,59]

A comparison between the presented "X-ray reflectivity" (Figure 3) and "in-plane 1D GISAXS profiles" (Figure 4) indicates a direct relation between surface roughness and ordered nanodomains. Accordingly, we suggest the following scenario. The PS block of P(S-*b*-MMA) segregates preferably to a PS brush whereas the PMMA block segregates to a PMMA layer and a hydrophilic surface of a SiO_x/Si substrate.[60] The block with smaller surface tension, PS, segregates to the vacuum interface. As the PMMA block is minor ($f_{PMMA} = 0.28\%$), the preferred wetting of PMMA blocks on the entire flat surface of SiO_x/Si or PMMA-SiO_x/Si substrates incurs a large entropic penalty. This penalty results from an autophobic effect according to which a monolayer of P(S-*b*-MMA) anchoring on SiO_x/Si or PMMA-SiO_x/Si adopts a brush conformation.[43] Upon heating, the entropic penalty causes the undulation of the film thickness. The initial thickness of a thin spin-coated film is comparable with the intercylinder period of a P(S-*b*-MMA) bulk sample. Thus, for the surface-modified substrates grafted with a PS monolayer, thin P(S-*b*-MMA) films might remain stable because of the preferential wetting of PS blocks with both interfaces (symmetric wetting). We speculate that barriers to form islands or holes are great, which explains why a low density of holes is present in the thin films on the PS-SiO_x/Si substrates. In contrast, mild dewetting of thin films on a PS brush was obtained on the same time scale of annealing, for which severe dewetting of thin films on the SiO_x/Si and PMMA-SiO_x/Si substrates was obtained. Although a brush conformation of the underlying PS layer might result in an entropic repulsion for the PS blocks, exerting a driving force to deform the P(S-*b*-MMA) films, the large resisting force at the PS-block/PS-brush interface decreases the rate of dewetting of thin films. We attribute the large resisting force to a greater viscosity of the PS block than of the underlying PS brush anchored on SiO_x/Si as the molecular mass of the PS block is greater than that of PS−OH, which has the same molar mass as PMMA−OH, 6 kg/mol, much less than M_e. As the PMMA block has a preferred interaction with hydrophilic surfaces having polar groups, autophobic dewetting occurs within the thin films on SiO_x/Si, on top of which was absorbed a monolayer of P(S-*b*-MMA) with the PMMA block absorbing at the film/substrate surface and the PS block facing upward. Consequently, a nongrafted PS block within P(S-*b*-MMA) dewets a "brush" monolayer of its own species with a small dewetting velocity. The velocity of film rupture is thus smaller for the films on PS-SiO_x/Si than on PMMA-SiO_x/Si and SiO_x/Si. As a result, the films on PS-SiO_x/Si lack a large density of holes. We hence speculate that small grains with a short nanodomain correlation length as result of a perturbation of the nanodomain periodicity are present in some areas of the thin films on PS-SiO_x/Si.[27−29,58,60] In contrast, the films that significantly dewet on top of SiO_x/Si and PMMA-SiO_x/Si are expected to have large grains with a long nanodomain correlation length. Such a speculation is supported by the AFM images of Figure 5, in which the P(S-*b*-MMA) film on PS-SiO_x/Si reveals smaller gain size of the nanodomains than that on PMMA-SiO_x/Si. On the other hand, close scrutiny of the AFM topography (Figure 5c) indicates that the free surface of the intact film having small monograins seems very rough.

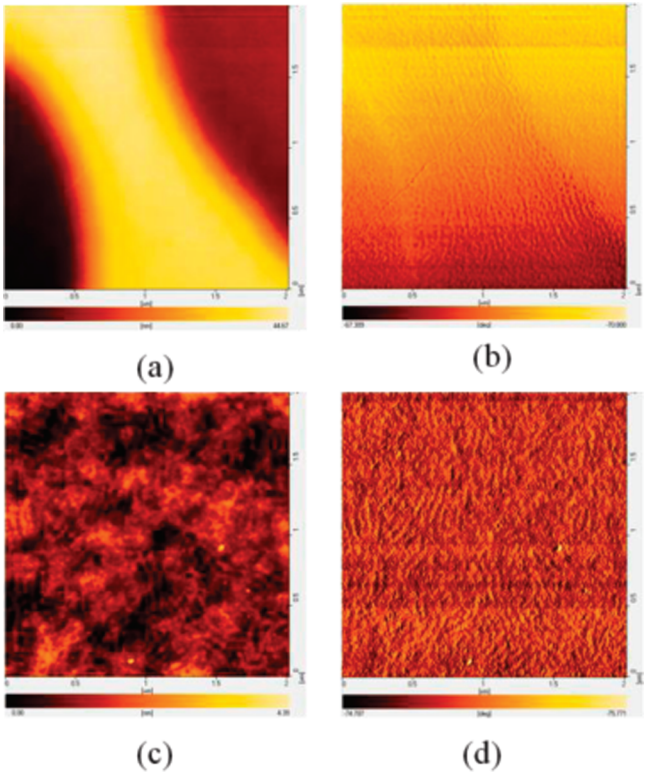

Figure 5. 2 μm × 2 μm AFM height images (a, c) and phase images (b, d) for P(S-*b*-MMA) films of initial thickness 34.3 nm spread on PMMA-SiO_x/Si (top images) and PS-SiO_x/Si (bottom images), after annealing.

To determine quantitatively the roughness of the free surface, we undertook further AFM roughness measurements on the free surfaces. The measured root-mean-square (rms) surface roughness was obtained by carrying out 10-time AFM measurements on each sample, and the statistic values are summarized in Figure 6a. Also, to clearly visualize the roughness contour, the cross sections through the air−polymer interfaces (air/nonanchored P(S-*b*-MMA) and air/grafted PS) of a film of initial thickness 36.4 nm on PS-SiO_x/Si, are also shown in Figure 6b,c. As shown in Figure 6a, the anchored and nonanchored P(S-*b*-MMA) layers in the destabilized films on polar substrates have a smooth free surface. Their rms surface roughness ranges from 0.2 to 0.5 nm. Similarly, the free surface of the grafted PS brush is smooth. By contrast, the free interface of the nonanchored P(S-*b*-MMA) layer on PS-SiO_x/Si has a rough free surface, evidenced by high rms roughness values in the

range of 0.8−1.2 nm. The driving force for surface roughening is that an excess of polymer chains that are excluded from grain boundaries between small monograins exhibits a high tendency to segregate onto the free surface to minimize the interfacial energy, yielding a grainy surface as displayed in Figure 6b. It is high likely that the nonanchored P(S-*b*-MMA)/grafted PS interface still remains a smooth surface since the segregation of the excess chains to the interface is difficult because of confinement. Therefore, the difference in rms roughness thickness between the two interfaces explains rapid damping of the high-frequency oscillations in X-ray reflectivity observed for P(S-*b*-MMA) films on PS-SiO_x/Si.

Roughness Correlation between Interfaces. To acquire further insight into the roughness replication of thin films, we performed diffuse X-ray scattering. One-dimensional GISAXS intensity profiles as a function of q_z, extracted from 2D X-ray scattering patterns with an out-of-plane scan cut, are shown in Figure 7. Several modulations due to resonant diffuse scattering are observable for the films on SiO_x/Si and PMMA-SiO_x/Si (Figure 7A,B). The wavelength of the modulations intrinsically depends on the spacing between both correlated interfaces.[56] According to the wavelength of the observed oscillations, the estimated length of ca. 22 nm is attributed to the thickness of the anchored P(S-*b*-MMA) monolayer. Thus, the presence of the modulations indicates that, on SiO_x/Si and PMMA-SiO_x/Si, the anchored P(S-*b*-MMA) monolayer has an interfacial roughness correlation. The amplitude of modulations can be regarded as an indication of the extent of interfacial roughness correlation since the mean electron density of the anchored monolayer remains unchanged.[61] A comparison of the amplitude of the observed modulations for the films on polar substrates demonstrates that the extent of roughness correlation for the anchored P(S-*b*-MMA) monolayer covered by droplets is relatively small.

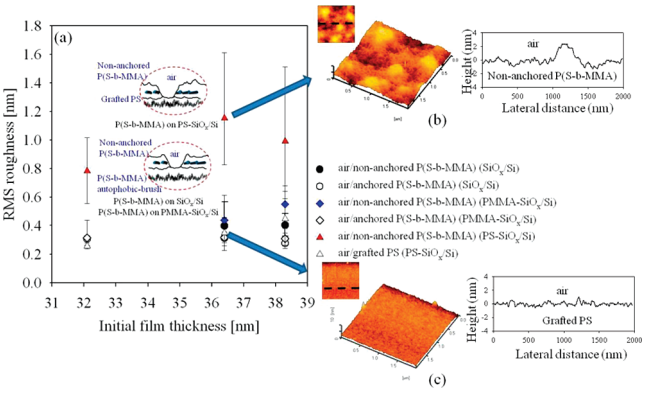

Figure 6. (a) The rms surface roughness of various air/polymer interfaces (air/nonanchored P(S-*b*-MMA), air/anchored P(S-*b*-MMA), and air/grafted PS) for P(S-*b*-MMA) films of initial thickness 32.1, 36.4, and 38.3 nm on SiO_x/Si, PMMA-SiO_x/Si, and PS-SiO_x/Si, after annealing. Inset shows the schematic illustration of the air/polymer interfaces. $2 \times 2\ \mu m^2$ 2D and 3D AFM images and corresponding cross sections of the air/nonanchored P(S-*b*-MMA) (b) and air/grafted PS (c) interfaces of an annealed P(S-*b*-MMA) film on PS-SiO_x/Si are shown for comparison. The cross sections were generated by choosing a random scan line. Dotted lines were plotted for guiding the eyes.

In contrast, the top layer of nonanchored P(S-*b*-MMA) exhibits a different behavior, namely, the complete absence of roughness correlation. Müller-Buschbaum et al. demonstrated that the roughness conformability is metastable and that annealing at temperatures far above T_g produce a decay of interfacial correlation in thin homopolymer films as the increased polymer mobility suffices to remove the roughness correlation.[42] At the stage, the surface roughness was controlled by thermal fluctuations at the liquid surface. Sufficient thermal annealing at high temperatures causes various dewetting patterns that reflect variations in the film thickness. The relaxation period for the loss of roughness correlation was less than the time scale for dewetting.[42] In our work, on heating, various dewetting morphologies (islands and holes) of the BCP thin films on the SiO_x/Si and PMMA-SiO_x/Si substrates were observed in optical micrographs of these films. Therefore, the roughness correlation of the top layer of nonanchored P(S-*b*-MMA) chains significantly vanished during dewetting. Regardless of the versatile surface morphologies induced by various dewetting mechanisms, the anchored P(S-*b*-MMA) brushlike monolayer on both SiO_x/Si and PMMA-SiO_x/Si substrates has a roughness correlation. However, the interfacial roughness correlation may not reach an equilibrium state. Upon heating far above the T_gs of the PS and PMMA blocks the interfacial roughnesses of the anchored P(S-*b*-MMA) monolayer should be independent, rather than correlated since the relaxation rate for suppressing surface roughness is different between free PS chains and tethered PMMA chains. After annealing, the interfacial roughnesses for the two layers (anchored and nonanchored P(S-*b*-MMA)) should be in an analogous matter (i.e., significant decay of roughness correlation). We ascribe the presence of roughness correlation to retardation in the decay rate for the wetting layer since the extent of the roughness correlation observed here depends upon the time scale over which the annealing was achieved. Wang et al. found that at an attractive solid surface the interactions between the film and the substrate led the film into a confined, viscous gel-type state.[62] Thus, the time scale of

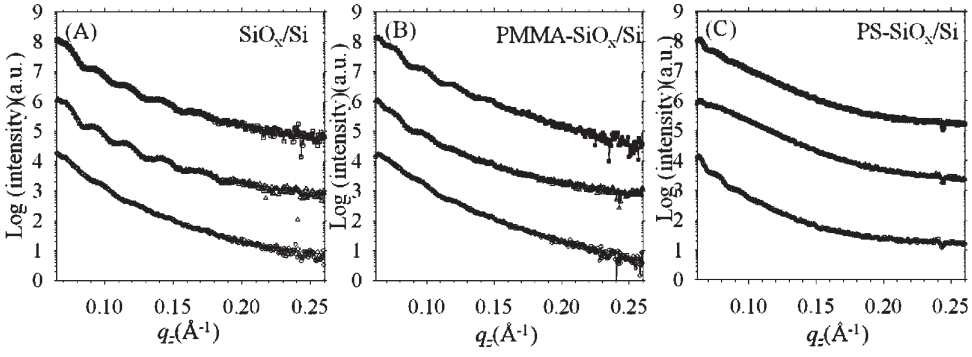

Figure 7. 1D out-of-plane profiles of GISAXS for P(S-*b*-MMA) films of initial thickness 32.1 nm (bottom curves), 36.4 nm (middle curves), and 38.3 nm (top curves), spread on substrates of three kinds: (A) SiO_x/Si, (B) PMMA-SiO_x/Si, and (C) PS-SiO_x/Si, after annealing. For clarity, the curves are shifted relative to each other by 1 decade.

removing roughness correlation by annealing is taken much longer for the anchored P(S-*b*-MMA) wetting layer.

In addition to the solid substrate surface having the effect of retarding the decay of roughness correlation, there is another effect in the vicinity of the free interface that should be considered as well.[63,64] Kerle et al. investigated that the roughness relaxations of the top PS surface under different boundary conditions.[64] They found that "air" acted like a poor solvent for PS and that a large amount of PS chains in contact with air led to a liquidlike behavior of the PS surface layer. Capping a "passive" layer on top to reduce interfacial energies and to prevent the amount of exposed surface area from air would significantly retard the extent and rate of roughness relaxation.[64] This explanation also accounts for the behavior observed here. The extent of interfacial roughness correlation of the P(S-*b*-MMA) wetting monolayer covered by droplets was comparatively low. The reason is that as a high density of droplets yielded by dewetting, the amount of surface area of the underlying P(S-*b*-MMA) wetting layer increased to be in contact with air, facilitating the relaxation of the PS blocks of the wetting layer.

To compare the decay of roughness correlation in the P(S-*b*-MMA) thin films on the PS-SiO_x/Si substrates, we also performed out-of-plane cuts on the 2D GISAXS patterns. As shown in Figure 7C, the low-frequency fringes attributed to the layer thickness of PS brushes are observable, whereas the high-frequency fringes are strongly damped. This damping is taken to indicate the absence of an interfacial correlation at the both interfaces of P(S-*b*-MMA) films. In contrast, the correlated roughness of PS brushes is preserved after heating, indicating retardation of the coating of P(S-*b*-MMA) on the conformal roughness of the underlying PS sublayer.

Conclusion

We demonstrated that commensurability effects play an important role in not only the ordering of cylindrical nanodomains but also the roughness at interfaces. At the stage of spin-coating, P(S-*b*-MMA) thin films effectively wet SiO_x/Si, PMMA-SiO_x/Si, and PS-SiO_x/Si substrates. On substrates with hydrophilic groups, upon annealing the films of which the initial thickness is incommensurate with the spacing of nanodomains become metastable and dewet to form relief microstructures (holes and islands) on a monolayer of autophobically induced P(S-*b*-MMA) brush. As the commensurability is achieved with an undulation of the surface thickness, the relief structures have a smooth surface and ordered cylindrical nanodomains. Their interfaces have identical mean roughness thickness but are not correlated in roughness contour. In comparison, the underlying P(S-*b*-MMA) wetting layer still reveals a correlation roughness after annealing. The decay of roughness correlation in response to annealing depends on not only attractive surfaces on a solid but also interfacial energies in the vicinity of free surface. Furthermore, the films on PS-SiO_x/Si reveal distinct morphologies. As the initial thickness is closely commensurate for symmetric segregating of the PS block on both interfaces, a low density of holes is present because the energy barrier of dewetting to form the relied microstructures is large so that the large-scale undulations in film thicknesses are prohibited. The films on PS-SiO_x/Si consequently reveal a rough surface that differs from the substrate surface and have small monograins that yielded as a result of chain stretching. The small-scale surface roughening arises from preferential segregation of certain chains excluded from monograin boundaries onto the free interface.

Acknowledgment. The National Science Council provided support (NSC 97-2218-E-008-011-MY2). We thank Dr. U-Ser Jeng, Dr. Chiu-Hun Su, and Dr. Chun-Jen Su for their assistance in the GISAXS experiments at beamline BL23A at the NSRRC and Mr. Er-Chiang Chen for assistance in measuring X-ray reflectivity at National Chung Hsing University. Thanks should also be due to the referees, whose comments/suggestions have further improved the contents and style of this paper. Their helpful and constructive tips are now an integral part in the final text.

Supporting Information Available: Static water contact angles on the substrates (Figure S1), reflection optical micrographs (Figure S2), X-ray reflectivity data (Figure S3) of P(S-*b*-MMA) films as spun on substrates without thermal annealing, and 2D GISAXS data (Figure S4) for the annealed thin films. This material is available free of charge via the Internet at http://pubs.acs.org.

References and Notes

(1) Park, M.; Harrison, C.; Chaikin, P. M.; Register, R. A.; Adamson, D. H. *Science* **1997**, *276*, 1401–1404.
(2) Li, R. R.; Dapkus, P. D.; Thompson, M. E.; Jeong, W. G.; Harrison, C.; Chaikin, P. M.; Register, R. A.; Adamson, D. H. *Appl. Phys. Lett*. **2000**, *76*, 1689–1691.
(3) Cheng, J. Y.; Ross, C. A.; Chan, V. Z. H.; Thomas, E. L.; Lammertink, R. G. H.; Vancso, G. J. *Adv. Mater*. **2001**, *13*, 1174–1178.
(4) Kim, S. O.; Solak, H. H.; Stoykovich, M. P.; Ferrier, N. J.; de Pablo, J. J.; Nealey, P. F. *Nature* **2003**, *424*, 411–414.
(5) Stoykovich, M. P.; Kang, H.; Daoulas, K. C.; Liu, G.; Liu, C. C.; de Pablo, J. J.; Müller, M.; Nealey, P. F. *ACS Nano* **2007**, *1*, 168–175.
(6) Thurn-Albrecht, T.; Schotter, J.; Kastle, C. A.; Emley, N.; Shibauchi, T.; Krusin-Elbaum, L.; Guarini, K.; Black, C. T.; Tuominen, M. T.; Russell, T. P. *Science* **2000**, *290*, 2126–2129.
(7) Thurn-Albrecht, T.; Steiner, R.; DeRouchey, J.; Stafford, C. M.; Huang, E.; Bal, M.; Tuominen, M.; Hawker, C. J.; Russell, T. P. *Adv. Mater*. **2000**, *12*, 787–791.
(8) Lopes, W. A.; Jaeger, H. M. *Nature* **2001**, *414*, 735–738.
(9) Segalman, R. A.; Yokoyama, H.; Kramer, E. J. *Adv. Mater*. **2001**, *13*, 1152–1155.
(10) Cheng, J. Y.; Ross, C. A.; Thomas, E. L.; Smith, H. I.; Vancso, G. J. *Appl. Phys. Lett*. **2002**, *81*, 3657–3659.
(11) Reiter, G.; Castelein, G.; Hoerner, P.; Riess, G.; Blumen, A.; Sommer, J. U. *Phys. Rev. Lett*. **1999**, *83*, 3844–3847.
(12) De Rosa, C.; Park, C.; Thomas, E. L.; Lotz, B. *Nature* **2000**, *405*, 433–437.
(13) Tseng, W. H.; Hsieh, P. Y.; Ho, R. M.; Huang, B. H.; Lin, C. C.; Lotz, B. *Macromolecules* **2006**, *39*, 7071–7077.
(14) Ho, R. M.; Hsieh, P. Y.; Tseng, W. H.; Lin, C. C.; Huang, B. H.; Lotz, B. *Macromolecules* **2003**, *36*, 9085–9092.
(15) Mansky, P.; Liu, Y.; Huang, E.; Russell, T. P.; Hawker, C. J. *Science* **1997**, *275*, 1458–1460.
(16) Huang, E.; Rockford, L.; Russell, T. P.; Hawker, C. J. *Nature* **1998**, *395*, 757–758.
(17) Rockford, L.; Liu, Y.; Mansky, P.; Russell, T. P.; Yoon, M.; Mochrie, S. G. J. *Phys. Rev. Lett*. **1999**, *82*, 2602–2605.
(18) Rockford, L.; Mochrie, S. G. J.; Russell, T. P. *Macromolecules* **2001**, *34*, 1487–1492.
(19) Kim, G.; Libera, M. *Macromolecules* **1998**, *31*, 2569–2577.
(20) Kim, G.; Libera, M. *Macromolecules* **1998**, *31*, 2670–2672.
(21) Kim, S. H.; Misner, M. J.; Xu, T.; Kimura, M.; Russell, T. P. *Adv. Mater*. **2004**, *16*, 226–231.
(22) Knoll, A.; Horvat, A.; Lyakhova, K. S.; Krausch, G.; Sevink, G. J. A.; Zvelindovsky, A. V.; Magerle, R. *Phys. Rev. Lett*. **2002**, *89*, 035501–035504.
(23) Horvat, A.; Lyakhova, K. S.; Sevink, G. J. A.; Zvelindovsky, A. V.; Magerle, R. *J. Chem. Phys*. **2004**, *120*, 1117–1126.
(24) Coulon, G.; Russell, T. P.; Deline, V. R.; Green, P. F. *Macromolecules* **1989**, *22*, 2581–2589.
(25) Anastasiadis, S. H.; Russell, T. P.; Satija, S. K.; Majkrzak, C. F. *Phys. Rev. Lett*. **1989**, *62*, 1852–1855.
(26) Henkee, C. S.; Thomas, E. L.; Fetters., L. J. *J. Mater. Sci*. **1988**, *23*, 1685–1694.
(27) Lambooy, P.; Russell, T. P.; Kellogg, G. J.; Mayes, A. M.; Gallagher, P. D.; Satija, S. K. *Phys. Rev. Lett*. **1994**, *72*, 2899–2902.
(28) Koneripalli, N.; Singh, N.; Levicky, R.; Bates, F. S.; Gallagher, P. D.; Satija, S. K. *Macromolecules* **1995**, *28*, 2897–2904.

(29) Mansky, P.; Russell, T. P.; Hawker, C. J.; Pitsikalis, M.; Mays, J. *Macromolecules* **1997**, *30*, 6810–6813.
(30) Kellogg, G. J.; Walton, D. G.; Mayes, A. M.; Lambooy, P.; Russell, T. P.; Gallagher, P. D.; Satija, S. K. *Phys. Rev. Lett.* **1996**, *76*, 2503–2506.
(31) Huang, E.; Russell, T. P.; Harrison, C.; Chaikin, P. M.; Register, R. A.; Hawker, C. J.; Mays, J. *Macromolecules* **1998**, *31*, 7641–7650.
(32) Reiter, G.; Hamieh, M.; Damman, P.; Sclavons, S.; Gabriele, S.; Vilmin, T.; Raphael, E. *Nat. Mater.* **2005**, *4*, 754–758.
(33) Vrij, A. *Discuss. Faraday Soc.* **1966**, *42*, 23–33.
(34) Wyart, F. B.; Martin, P.; Redon, C. *Langmuir* **1993**, *9*, 3682–3690.
(35) Reiter, G. *Phys. Rev. Lett.* **2001**, *87*, 186101−1–186101−4.
(36) Xie, R.; Karim, A.; Douglas, J. F.; Han, C. C.; Weiss, R. A. *Phys. Rev. Lett.* **1998**, *81*, 1251–1254.
(37) Sharma, A.; Khanna, R. *Phys. Rev. Lett.* **1998**, *81*, 3463–3466.
(38) Sharma, A.; Khanna, R. *J. Chem. Phys.* **1999**, *110*, 4929–4936.
(39) Müller-Buschbaum, P. *J. Phys.: Condens. Matter* **2003**, *15*, R1549–R1582.
(40) Geoghegan, M.; Krausch, G. *Prog. Polym. Sci.* **2003**, *28*, 261–302.
(41) Müller-Buschbaum, P.; Gutmann, J. S.; Lorenz, C.; Schmitt, T.; Stamm, M. *Macromolecules* **1998**, *31*, 9265–9272.
(42) Müller-Buschbaum, P.; Stamm, M. *Macromolecules* **1998**, *31*, 3686–3692.
(43) Limary, R.; Green, P. F. *Langmuir* **1999**, *15*, 5617–5622.
(44) Limary, R.; Green, P. F. *Macromolecules* **1999**, *32*, 8167–8172.
(45) Masson, J. L.; Limary, R.; Green, P. F. *J. Chem. Phys.* **2001**, *114*, 10963–10967.
(46) Green, P. F.; Limary, R. *Adv. Colloid Interface Sci.* **2001**, *94*, 53–81.
(47) Müller-Buschbaum, P.; Gutmann, J. S.; Lorenz-Haas, C.; Wunnicke, O.; Stamm, M.; Petry, W. *Macromolecules* **2002**, *35*, 2017–2023.
(48) Tsarkova, L.; Knoll, A.; Krausch, G.; Magerle, R. *Macromolecules* **2006**, *39*, 3608–3615.
(49) Black, C. T.; Ruiz, R.; Breyta, G.; Cheng, J. Y.; Colburn, M. E.; Guarini, K. W.; Kim, H. C.; Zhang, Y. *IBM J. Res. Dev.* **2007**, *51*, 605–633.
(50) Han, E.; Stuen, K. O.; La, Y. H.; Nealey, P. F.; Gopalan, P. *Macromolecules* **2008**, *41*, 9090–9097.
(51) Ham, S.; Shin, C.; Kim, E.; Ryu, D. Y.; Jeong, U.; Russell, T. P.; Hawker, C. J. *Macromolecules* **2008**, *41*, 6431–6437.
(52) Jeng, U. S.; Su, C. H.; Su, C. J.; Liao, K. F.; Chuang, W. T.; Lai, Y. H.; Chang, J. W.; Chen, Y. J.; Huang, Y. S.; Lee, M. T.; Yu, K. L.; Lin, J. M.; Liu, D. G.; Chang, C. F.; Liu, C. Y.; Chang, C. H.; Liang, K. S. *J. Appl. Crystallogr.* **2010**, *43*, 110–121.
(53) Lee, B.; Park, I.; Yoon, J.; Park, S.; Kim, J.; Kim, K. W.; Chang, T.; Ree, M. *Macromolecules* **2005**, *38*, 4311–4323.
(54) Müller-Buschbaum, P. *Anal. Bioanal. Chem.* **2003**, *376*, 3–10.
(55) The intercylinder distance (D) of a P(S-*b*-MMA) bulk sample was determined to be 37.65 nm based on $D = (4/3)^{1/2} d_{100}$, where $d_{100} = 2\pi/q_{100}$ and $q_{100} = 0.0193$ Å^{-1}, by means of SAXS with X-ray of an energy of 8 keV .
(56) Shin, K.; Pu, Y.; Rafailovich, M. H.; Sokolov, J.; Seeck, O. H.; Sinha, S. K.; Tolan, M.; Kolb, R. *Macromolecules* **2001**, *34*, 5620–5626.
(57) Koneripalli, N.; Bates, F. S.; Fredrickson, G. H. *Phys. Rev. Lett.* **1998**, *81*, 1861–1864.
(58) Stein, G. E.; Lee, W. B.; Fredrickson, G. H.; Kramer, E. J.; Li, X.; Wang, J. *Macromolecules* **2007**, *40*, 5791–5800.
(59) Mansky, P.; Russell, T. P.; Hawker, C. J.; Mays, J.; Cook, D. C.; Satija, S. K. *Phys. Rev. Lett.* **1997**, *79*, 237–240.
(60) Hammond, M. R.; Cochran, E.; Fredrickson, G. H.; Kramer, E. J. *Macromolecules* **2005**, *38*, 6575–6585.
(61) Müller-Buschbaum, P.; Gutmann, J. S.; Wolkenhauer, M.; Kraus, J.; Stamm, M.; Smilgies, D.; Petry, W. *Macromolecules* **2001**, *34*, 1369–1375.
(62) Wang, J.; Tolan, M.; Seeck, O. H.; Sinha, S. K.; Bahr, O.; Rafailovich, M. H.; Sokolov, J. *Phys. Rev. Lett.* **1999**, *83*, 564–567.
(63) Kajiyama, T.; Tanaka, K.; Takahara, A. *Macromolecules* **1995**, *28*, 3482–3484.
(64) Kerle, T.; Lin, Z. Q.; Kim, H. C.; Russell, T. P. *Macromolecules* **2001**, *34*, 3484–3492.